

Chest X-ray Foundation Model with Global and Local Representations Integration

Zefan Yang, Xuanang Xu, Jiajin Zhang, Ge Wang, *Fellow, IEEE*,
Mannudeep K. Kalra, and Pingkun Yan, *Senior Member, IEEE*

Abstract—Chest X-ray (CXR) is the most frequently ordered imaging test, supporting diverse clinical tasks from thoracic disease detection to postoperative monitoring. However, task-specific classification models are limited in scope, require costly labeled data, and lack generalizability to out-of-distribution datasets. To address these challenges, we introduce CheXFound, a self-supervised vision foundation model that learns robust CXR representations and generalizes effectively across a wide range of downstream tasks. We pretrain CheXFound on a curated CXR-1M dataset, comprising over one million unique CXRs from publicly available sources. We propose a Global and Local Representations Integration (GLoRI) module for downstream adaptations, by incorporating disease-specific local features with global image features for enhanced performance in multilabel classification. Our experimental results show that CheXFound outperforms state-of-the-art models in classifying 40 disease findings across different prevalence levels on the CXR-LT 24 dataset and exhibits superior label efficiency on downstream tasks with limited training data. Additionally, CheXFound achieved significant improvements on new tasks with out-of-distribution datasets, including opportunistic cardiovascular disease risk estimation and mortality prediction. These results highlight CheXFound’s strong generalization capabilities, enabling diverse adaptations with improved label efficiency. The project source code is publicly available at <https://github.com/RPIDIAL/CheXFound>.

Index Terms—Chest X-ray, Foundation Model, Knowledge Distillation, Self-supervised Learning, Pretraining.

I. INTRODUCTION

CHEST X-ray (CXR) is one of the most commonly ordered imaging tests worldwide [1]. Clinical CXR interpretation encompasses a broad spectrum of tasks, including detecting diseases associated with the lungs, heart, blood vessel, and bones, as well as monitoring postoperative recovery and the positioning of support devices. With advancements in

Z. Yang, X. Xu, G. Wang, and P. Yan* are with the Department of Biomedical Engineering and Center for Biotechnology and Interdisciplinary Studies, Rensselaer Polytechnic Institute, Troy, NY, USA.

J. Zhang was with the Department of Biomedical Engineering and Center for Biotechnology and Interdisciplinary Studies, Rensselaer Polytechnic Institute, when he contributed to this work.

M. K. Kalra is with the Department of Radiology, Massachusetts General Hospital, Harvard Medical School, Boston, MA, USA.

This research was funded in part by the NSF CAREER award 2046708 and the NIA Predoctoral Training Program For Alzheimer’s Disease At The Interface Of Data Science, Engineering And Biology Training Program T32AG078123.

*Corresponding author: yanp2@rpi.edu

computer-aided diagnosis, these tasks now extend even further to include opportunistic disease risk assessment, such as cardiovascular disease [2], [3], mortality risk [4], and diabetes [5], among other factors not directly quantifiable by human eyes. Training specialized classification models for each task from scratch poses significant limitations. Such models are typically effective only within a narrow scope of pathologies and struggle to generalize to out-of-distribution datasets. Furthermore, developing these models requires extensive labeled datasets, which are both cost-prohibitive and inefficient. These challenges underscore the need for self-supervised models that can learn robust representations and demonstrate superior generalization capabilities across diverse tasks.

Recent advancements in the field of computer vision [6]–[9] demonstrate that self-supervised vision models can produce task-agnostic and semantic-rich image representations that achieve improved performance on a broad spectrum of downstream tasks. Such models are called foundation models because of their superior capabilities to adapt to diverse downstream tasks when pretrained on large-scale data. Recent works in self-supervised learning for CXR interpretation adopt a series of advanced training strategies to learn high-quality image representations, including contrastive learning [10], masked image modeling (MIM) [11], and self-distillation [12]. Research further use CXRs and their clinical reports to perform contrastive language-image pretraining [13]. However, these studies have two major limitations. First, they only evaluate model performance for classifying a narrow range of disease findings, without considering the long-tail nature of pathologies in CXR and the opportunistic CXR interpretation tasks, such as cardiovascular disease (CVD) risk estimation and mortality prediction. Second, these studies simply rely on the global image features for disease classification, overlooking the use of CXR representations learned by the foundation models to provide disease-specific local features to enhance performance. Addressing these limitations is pivotal to the development of the CXR foundation models towards clinical applications which often involve interpreting a wide range of disease findings. It also has broader implications by enabling CVD risk estimation and mortality prediction with a routine CXR.

In this work, we introduce CheXFound, a vision foundation model specialized for CXR image analysis that learns high-quality CXR representations and generalizes effectively across a wide range of thoracic disease classification and opportunistic

tic risk estimation tasks. We pretrain CheXFound on a curated CXR-1M dataset, comprising more than one million unique CXRs from 13 publicly available datasets, including MIMIC-CXR [14], CheXpert [15], PadChest [16], CXR14 [17], BRAX [18], VinDr-CXR [19], and CANDID-PTX [20], among others. Our CheXFound model is pretrained via DINOv2 [21], a state-of-the-art self-supervised learning method with strong off-the-shelf linear probe performance. For downstream adaptation, we propose a Global and Local Representations Integration (GLoRI) module. GLoRI is trained on top of the frozen CheXFound model. It uses the attentional principle to compute disease-specific local features and integrates them with the global image features to improve the multilabel classification performance.

We assess CheXFound’s performance on two tiers of CXR interpretation tasks, including thoracic disease classification and opportunistic risk estimation. CheXFound outperforms previous state-of-the-art models such as RAD-DINO [12], EVA-X [11], and CheXzero [13] across 40 disease findings at different prevalence levels on the CXR-LT 24 dataset [22]. Besides, CheXFound demonstrates superior label efficiency, which achieves best-performing results on the Shenzhen, Montgomery, and JSRT datasets with limited training data. We also find that CheXFound achieves significant performance increases compared with its comparisons for the out-of-distribution tasks, including opportunistic CVD risk estimation and mortality prediction on the PLCO dataset [23]. Overall, we demonstrate CheXFound’s strong generalization capabilities across a wide range of downstream tasks on in-distribution and out-of-distribution datasets. CheXFound’s strong representation quality can enable diverse downstream adaptations with improved label efficiency.

II. RELATED WORKS

A. Self-supervised Visual Representation Learning

Our study is mostly related to self-supervised visual representation learning. After the success of masked language modeling in language domain, masked autoencoder (MAE) [7] and BEiT [24] translate the idea into visual representation learning, which assume the pretext task of recovering masked pixels can train networks to learn visual information and context. Another family of self-supervised learning methods (SimCLR [25] and MoCov3 [6]) apply contrastive learning objectives, assuming augmentation invariance of image representations and aiming to learn contrastive class representations. These methods have been reported to achieve inferior linear probe performance and require fine-tuning backbone features [21]. They also do not translate well into medical applications [26]. Beyond the above methods, another family of self-supervised learning methods rely on a knowledge distillation framework first introduced by BYOL [27], which bootstraps latent features of a teacher network to train a student network. DINO [8] applies self-distillation with the Transformer architecture and enforce similarity of categorical distributions. iBOT [9] extends the framework with masked image modeling. DINOv2 [21] carefully curates pretraining data with deduplication and further makes modifications to improve training. Overall,

self-distillation methods excel at linear probe evaluation and have demonstrated generalizability in medical application [12], [26]. Our study follows this methodology to train CheXFound with strong representation quality.

B. Foundation Models for Medical Applications

The surge in available data and computational resources have enabled the large-scale pretraining of foundation models. Studies have demonstrated that scaling foundation models in data and model sizes can achieve performance increases across a wide array of downstream tasks [7], [21], [26]. In medical domain, research works have developed multiple categories of foundation models differing in technical approaches and data modalities. Our study is related to vision-centric foundation models. RAD-DINO [12] and EVA-X [11] are two foundation models in CXR domain. Compared to CheXFound with ViT-L pretrained on CXR-1M, these models are limited in model and data scales. Another category of foundation models incorporate vision and text data for multimodal pretraining. CheXzero [13], BiomedCLIP [28], PubMedCLIP [29] use contrastive vision-language pretraining, which is effective in zero-shot classification. Further development of vision-language models takes advantage of instruction-tuning to improve reasoning and detailed description capabilities [30]–[32]. Overall, research empirically finds that vision-language models achieve inferior performance than vision-centric foundation models in CXR classification [12]. In this study, we focus on the vision-centric foundation model and investigate its capability for extensive CXR classification tasks. To the best of our knowledge, our work employs the largest-scale self-supervised pretraining with over 1 million unique CXRs.

III. MATERIALS AND METHODS

A. CXR-1M for Pretraining CheXFound

As detailed in Table I, we curated the CXR-1M dataset for self-supervised pretraining by retrieving in total 1,005,733 unique CXRs from 13 publicly available datasets [14]–[20], [33]–[38] that were released for various downstream tasks, including disease diagnosis, abnormality detection, foreign objection detection, and segmentation. To learn comprehensive representations for multiview CXR analysis, both frontal-view in PA (posterior-anterior) or AP (anterior-posterior) and lateral-view CXRs were included into CXR-1M.

To evaluate the data scalability of self-supervised pretraining, we further created CXR-207K and CXR-744K, denoting two subsets of CXR-1M, as shown in Table I. CXR-207K contains approximately 207K CXRs from MIMIC-CXR. CXR-744K contains around 744K CXRs from five datasets: MIMIC-CXR, CheXpert, PadChest, CXR14, and BRAX.

We used DINOv2 [21], a state-of-the-art self-supervised learning method, to pretrain CheXFound on CXR-1M. DINOv2 inherits designs from DINO [8] and iBOT [9] and incorporates two self-distillation objectives: the masked image modeling loss \mathcal{L}_{MIM} and the [CLS] token alignment loss $\mathcal{L}_{\text{[CLS]}}$. It uses a teacher-student knowledge distillation architecture as shown in Fig. 1 to learn CXR representations. Masked image modeling uses the teacher network as an online

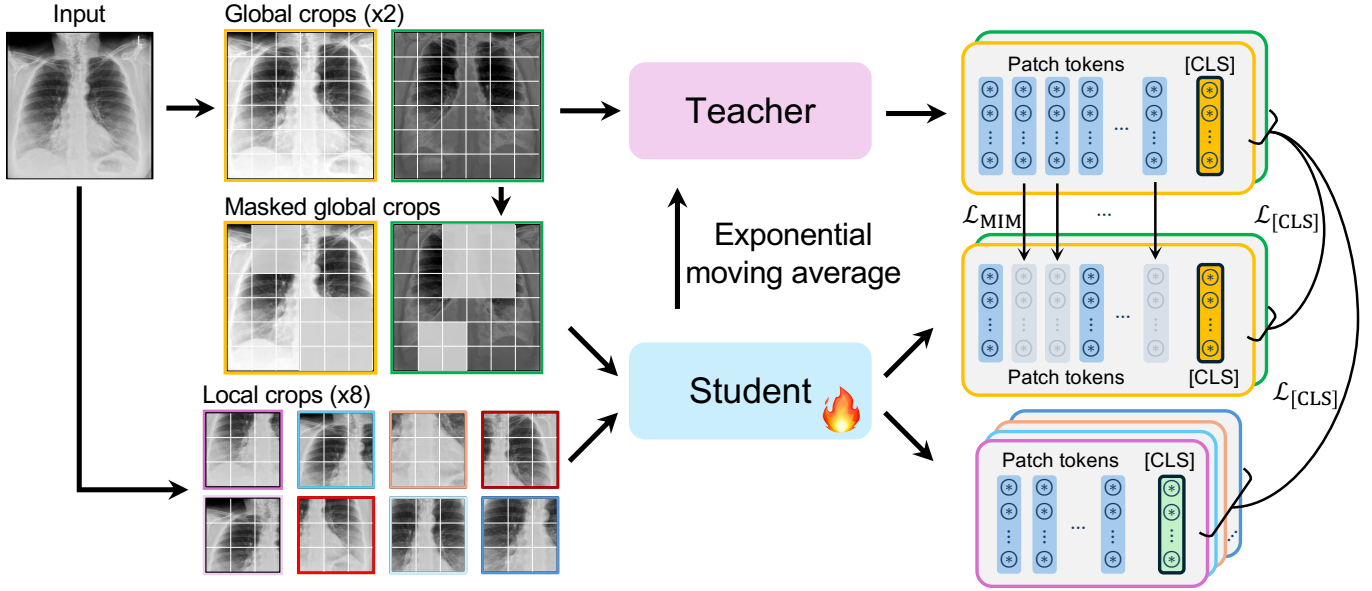


Fig. 1. Overview of self-supervised pretraining of CheXFound, using publicly available CXRs from multiple institutions with a masked image modeling objective and a [CLS] token alignment objective.

TABLE I

CURATION OF CXR-1M WITH PUBLICLY AVAILABLE DATASETS FROM DIVERSE INSTITUTIONS FOR SELF-SUPERVISED PRETRAINING. CXR-1M IS SUBSETTED INTO CXR-207K AND CXR-744K TO EVALUATE THE DATA SCALABILITY OF SELF-SUPERVISED MODELS.

Datasets	View	Findings	image #
MIMIC-CXR [14]	Frontal, Lateral	14 diseases	207,096
Total number of images in CXR-207K: 207,096			
CheXpert [15]	Frontal, Lateral	14 diseases	223,648
PadChest [16]	Frontal, Lateral	193 diseases	160,861
CXR14 [17]	Frontal	14 diseases	112,120
BRAX [18]	Frontal, Lateral	14 diseases	40,967
Total number of images in CXR-744K: 744,692			
VinDr-CXR [19]	Frontal	28 diseases	18,000
CANDID-PTX [20]	Frontal	Pneumothorax	19,237
SIIM-ACR [33]	Frontal	Pneumothorax	18,499
Object-CXR [34]	Frontal	Foreign objects	9,000
COVID-19 [35]	Frontal	COVID-19	7,597
COVIDx CXR-4 [36]	Frontal	COVID-19	84,818
MIDRC COVIDx [37]	Frontal	COVID-19	23,001
BIMCV COVID+ [38]	Frontal, Lateral	COVID-19	80,889
Total number of images in CXR-1M: 1,005,733			

tokenizer, which generates patch tokens from intact images to guide the student network in reconstructing masked patch tokens. This approach enables the student network to learn both visual features and contextual information effectively. On the other hand, the [CLS] token alignment loss $\mathcal{L}_{[CLS]}$ enforces similarity between [CLS] tokens output by the teacher and student networks. This approach aims to train the network to learn high-level class representations with off-the-shelf linear probe capabilities.

B. Global and Local Representation Integration for Multilabel Classification

For the downstream evaluation of CheXFound, the linear probe classifier is a pivotal tool to evaluate the quality of pretrained representations. However, the linear probe classifier has limited capability to address the multilabel classification problem commonly seen in CXR interpretation, since it generally relies on the global image features from a single [CLS] token for classifying a wide range of pathologies and lacks essential local details to support the predictions. In contrast, patch tokens from our pretrained CheXFound contain rich CXR representations and high-level contextual information learned via masked image modeling, which can provide disease-specific local features to substantially reduce ambiguities arisen from using the [CLS] token for classifying multiple pathologies. To take advantage of both local and global features for disease classification, we introduce GLoRI (Fig. 2), which utilizes a cross-attention layer with disease queries to summarize patch token features and a skip-connection to integrate the [CLS] token towards final prediction.

To be specific, GLoRI receives output patch tokens $\mathbf{u}^{\text{Patch}} \in \mathbb{R}^{N \times D_{\text{model}}}$ from the frozen CheXFound backbone as input, where D_{model} is the backbone embedding dimension. Since there can be a dimension mismatch between the backbone and GLoRI, we use a linear embedding layer to project $\mathbf{u}^{\text{Patch}}$ to the GLoRI dimensional space:

$$\mathbf{u}^{\text{Patch}} = \text{ReLU}(\text{Linear}^{\text{embed}}(\mathbf{u}^{\text{Patch}})), \quad (1)$$

where $\mathbf{u}^{\text{Patch}} \in \mathbb{R}^{N \times D_{\text{GLoRI}}}$ is the projected by the linear embedding layer $\text{Linear}^{\text{embed}}(\cdot)$ to the patch token sequence with dimension D_{GLoRI} . In GLoRI, to extract disease-specific local features using the cross-attention layer, we initialize M disease queries corresponding to M disease findings,

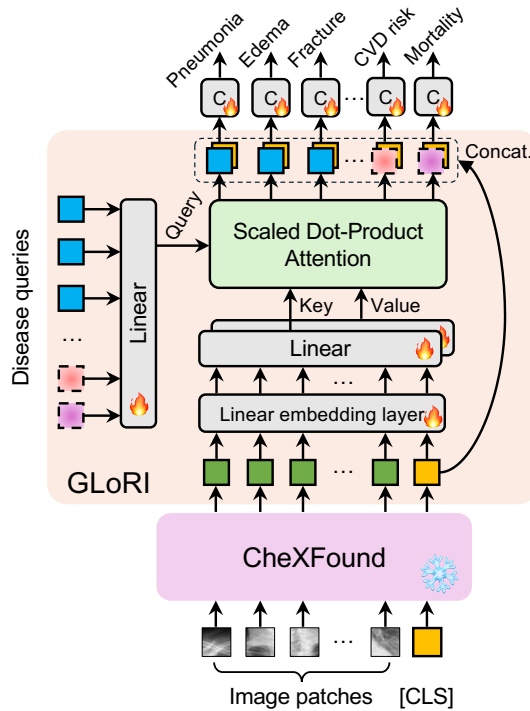


Fig. 2. Global and Local Representations Integration (GLoRI) for evaluating CheXFound on downstream tasks. GLoRI is appended on top of the frozen CheXFound backbone. GLoRI uses disease queries to compute attention-pooled CXR representations and integrates the global image features from [CLS] token for disease finding classification. For the opportunistic CXR interpretation, additional disease queries are created for GLoRI to retrieve representations related to the CVD risk estimation and mortality prediction.

denoted as $\mathbf{q} \in \mathbb{R}^{M \times D_{\text{key}}}$. The keys $\mathbf{k} \in \mathbb{R}^{M \times D_{\text{key}}}$ and values $\mathbf{v} \in \mathbb{R}^{M \times D_{\text{value}}}$ for the cross-attention layer are from $\mathbf{u}^{\text{Patch}}$, which provides rich CXR representations. A scaled dot-product attention module is used to compute attention-pooled features relevant to the query diseases:

$$\mathbf{q}' = \text{Softmax} \left(\frac{\text{Linear}^{\text{query}}(\mathbf{q}) \text{Linear}^{\text{key}}(\mathbf{k})^T}{\sqrt{D_{\text{key}}}} \right) \text{Linear}^{\text{value}}(\mathbf{v}), \quad (2)$$

where $\mathbf{q}' \in \mathbb{R}^{M \times D_{\text{key}}}$ denotes the output disease queries, which we consider contain disease-specific local features. D_{key} is the dimension of the key tokens. Last, we concatenate \mathbf{q}' with the [CLS] token to construct the GLoRI output token sequence. For multilabel classification, each GLoRI output token is projected by a linear classifier supervised by a binary cross-entropy loss.

Overall, GLoRI applies the attentional principle, which shares similarity with previous works, such as Perceiver [39] and DETR [40], for CheXFound’s downstream evaluation. We empirically demonstrate that GLoRI extracts local features relevant to disease abnormalities in CXRs in Section VI-A.

IV. EXPERIMENTAL DESIGN

A. Implementation Details

1) *Self-supervised pretraining details*: We conducted self-supervised pretraining of CheXFound on our curated CXR-1M

dataset (Table I) using the ViT-L architecture with a patch size of 16×16 pixels. The loss weights for $\mathcal{L}_{[\text{CLS}]}$ and \mathcal{L}_{MIM} were set to 1.0 and 3.0, respectively. The momentum to compute the exponential moving average of the student network was set to 0.994. We varied the global and local crop sizes to pretrain CheXFound at a range of resolutions. Specifically, we set the global and local crop size pairs to be (512, 144), (448, 128), (336, 128), and (224, 96). We set the number of global and local crops to 2 and 8, respectively. For masked image modeling, we set the proportion of masked patches to the range (0.1, 0.5). We trained CheXFound for 100 epochs with an epoch length of 2,500 iterations and a batch size of 14 per graphics processing unit (GPU). We used the AdamW optimizer with an initial learning rate of $2e-4$. We applied a Cosine annealing schedule for learning rate decay and a warm up period of 10 epochs. We pretrained CheXFound on a DGX-1 server with $8 \times$ NVIDIA A100 40GB GPUs. Depending on the image resolutions, the pretraining processes take around 48 to 96 hours. The project source code is publicly available at <https://github.com/RPIDIAL/CheXFound>.

2) *Downstream evaluation details*: In downstream evaluation, we trained GLoRI with feature representations from the frozen CheXFound. We took the concatenated representations from the last 4 layers of CheXFound as the input to GLoRI. We set the embedding dimension of GLoRI to 768. Disease queries were randomly initialized with a standard normal distribution. For the cross-attention layer, we used the multihead attention mechanism and set the number of heads to 8. To train GLoRI, we used the AdamW optimizer and conduct a thorough learning rate search in $\{1e-5, 2e-5, 5e-5, 1e-4, 2e-4, 5e-4, 1e-3, 2e-3, 5e-3\}$ to obtain the best-performing learning rate on the validation set. We then combined the training and validation sets for a second round of training using the best learning rate. To maximize the number of images that the GLoRI module processes during downstream adaptation, we trained GLoRI for 10 epochs on CXR-LT 24, CheXpert, and PLCO and 100 epochs on Shenzhen, Montgomery, and JSRT. We set the batch size to 16 for Montgomery and JSRT and 256 for CXR-LT 24, CheXpert, Shenzhen, and PLCO.

B. Experimental Design

To rigorously evaluate CheXFound’s in-distribution and out-of-distribution performance, we employed an extensive classification benchmark, consisting of in-distribution datasets (CXR-LT 24 [22] and CheXpert [15]) and out-of-distribution datasets (Shenzhen [41], Montgomery [41], Japanese Society of Radiological Technology (JSRT) [42], and Prostate, Lung, Colorectal, and Ovarian (PLCO) Cancer Screening Trial [23]). Following recent works in vision-centric foundation models [12], [26], we split the evaluation datasets into training, validation, and test splits. To avoid any potential data contamination, we included only the training set in CXR-LT 24 and the training and validation sets in CheXpert for self-supervised pretraining, while keeping the test set unseen. For the out-of-distribution datasets (Shenzhen, Montgomery, and JSRT), none of the images in the training, validation, and test sets were used for self-supervised pretraining.

Although the MIMIC-CXR dataset is the common benchmark to evaluate the performance of CXR interpretation models, its labels contain only 14 findings. To assess the generalizability of foundation models across diverse disease types, we conducted experiments on the CXR-LT 24 dataset which includes the annotations of 40 disease findings at different levels of prevalence (Fig. 4a). To evaluate the model performance, we divided CXR-LT 24 into a training set of 207,096 images and a test set of 51,775 images.

To evaluate the performance of the foundation models against the annotations on five selected pathologies (atelectasis, cardiomegaly, consolidation, edema, and pleural effusion) by board-certificated radiologists, we incorporated the CheXpert dataset. It was divided into 191,027 frontal-view images in the training set, 202 images in the validation set, and 518 images in the test set.

To assess the out-of-distribution generalization capabilities of the foundation models, we also performed evaluation on the Shenzhen and Montgomery datasets for tuberculosis detection and the JSRT database for lung nodule detection. The Shenzhen, Montgomery, and JSRT datasets were divided into training, validation, and test splits with a ratio of 70:10:20. Shenzhen contains 463 training images, 65 validation images, and 134 test images. Montgomery contains 96 training images, 14 validation images, and 28 test images. JSRT contains 171 training images, 24 validation images, and 50 test images.

To evaluate the extended predictive power of the foundation models, we obtained the lung screening CXRs from the PLCO trial and extracted the all-cause mortality and cardiovascular disease mortality labels from the up to 25-year follow-up data. The PLCO CXRs were divided into training, validation, and test sets of 133,543 images, 19,099 images, and 38,058 images respectively.

Since the CXR interpretation problem often involves severe class imbalance, we employed two metrics to evaluate model performance: the area under the precision-recall curve (AUPRC) and the area under the receiver operating characteristic curve (AUROC). For the multilabel classification problem, we computed the average of the metrics over disease findings. We estimated the 95% confidence intervals of the model performance in AUPRC and AUROC over 1,000 bootstrapped samples. To test statistical significance, we used a two-sided paired permutation test with 1,000 permutations to assess the observed performance differences of the two models for disease findings.

V. EXPERIMENTAL RESULTS

A. Overall performance comparison

A pivotal characteristic of foundation models lies in their capability to achieve improved performance on a wide range of downstream datasets. To evaluate the capability of foundation models, we compared CheXFound, which uses ViT-L pretrained on CXR-1M, with publicly available pretrained encoders, including RAD-DINO [12], EVA-X [11], CheXzero [13], BiomedCLIP [28], PubmedCLIP [29], and ConvNeXt [43]. RAD-DINO was pretrained on a combined dataset comprising MIMIC-CXR, CheXpert, PadChest, CXR14, and

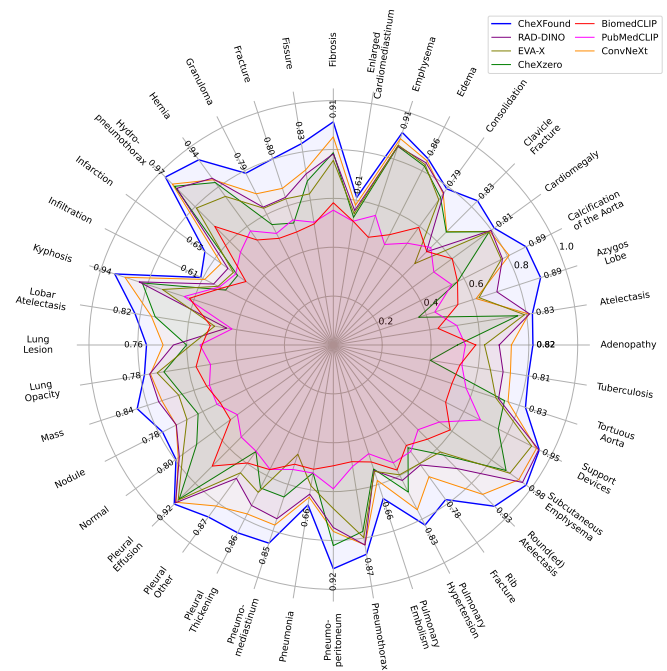


Fig. 3. Detailed Performance for 40 disease findings in AUROC on the CXR-LT 24 dataset. Our CheXFound is compared with the vision-centric foundation models (EVA-X and RAD-DINO), the vision-language pretrained foundation models (CheXzero, BiomedCLIP, and PubMedCLIP), and the end-to-end trained model (ConvNeXt) with ImageNet-22K pretraining.

BRAX, using the DINOv2 framework. EVA-X was pretrained on MIMIC-CXR, CheXpert, and CXR14 using EVA [44] technique with contrastive vision features for masked image modeling. CheXzero, a vision-language foundation model, was pretrained on MIMIC-CXR using contrastive language-image pretraining (CLIP) [45]. BiomedCLIP was pretrained on PMC-15M with image-text pairs collected from scientific articles. PubmedCLIP was initialized with the CLIP model and finetuned on PubMed articles. Finally, ConvNeXt was pretrained on the ImageNet-22K dataset.

To evaluate the effectiveness and generalizability of the representations extracted by the foundation models, we evaluated the linear probe performance across the five datasets (CXR-LT 24, CheXpert, Shenzhen, Montgomery, and JSRT). While linear probe provides a straightforward approach to evaluate the quality of representation, it primarily relies on global image features from the [CLS] token, often resulting in sub-optimal performance. Hence, we also evaluated the pretrained encoders using GLoRI, which incorporates attention-pooled local features in addition to the global image features from the [CLS] token. For vision-language pretrained encoders, we further validated the quality of their vision representations by examining their correlation with text features for disease finding classification.

Across all the five classification tasks (CXR-LT 24, CheXpert, Shenzhen, Montgomery, and JSRT), CheXFound consistently outperformed other foundation models in the linear probe setting as shown in Table II. On the multilabel, long-tailed classification task (CXR-LT 24), CheXFound achieved an AUPRC of 0.209, outperforming the next best-performing

TABLE II

COMPARISON CHEXFOUND AND OTHER FOUNDATION MODELS WHEN USING LINEAR PROBE AND GLoRI FOR CLASSIFICATION. VALUES INSIDE THE PARENTHESES INDICATE THE 95% CONFIDENCE INTERVALS. VALUES IN **BOLD** INDICATE THE BEST RESULTS.

Classifier	Foundation	CXR-LT 24		CheXpert		Shenzhen		Montgomery		JSRT	
		AUPRC	AUROC	AUPRC	AUROC	AUPRC	AUROC	AUPRC	AUROC	AUPRC	AUROC
Linear probe	PubMedCLIP [29]	0.089 _(.088–.089)	0.561 _(.554–.568)	0.277 _(.244–.311)	0.595 _(.564–.628)	0.857 _(.786–.913)	0.814 _(.738–.887)	0.565 _(.306–.817)	0.534 _(.310–.750)	0.785 _(.630–.912)	0.685 _(.511–.833)
	BiomedCLIP [28]	0.117 _(.116–.118)	0.643 _(.636–.649)	0.557 _(.504–.607)	0.841 _(.822–.860)	0.903 _(.843–.949)	0.885 _(.827–.934)	0.925 _(.791–1.0)	0.929 _(.822–1.0)	0.589 _(.427–.755)	0.432 _(.265–.601)
	CheXzero [13]	0.112 _(.111–.112)	0.552 _(.545–.558)	0.468 _(.424–.509)	0.778 _(.754–.798)	0.929 _(.884–.962)	0.906 _(.851–.950)	0.964 _(.869–1.0)	0.970 _(.898–1.0)	0.759 _(.597–.885)	0.620 _(.453–.777)
	EVA-X [11]	0.114 _(.113–.115)	0.596 _(.590–.602)	0.468 _(.422–.512)	0.788 _(.763–.812)	0.840 _(.738–.921)	0.824 _(.746–.898)	0.577 _(.320–.809)	0.509 _(.278–.749)	0.641 _(.472–.797)	0.490 _(.312–.660)
	RAD-DINO [12]	0.114 _(.113–.114)	0.557 _(.570–.583)	0.463 _(.422–.503)	0.746 _(.715–.778)	0.883 _(.818–.933)	0.861 _(.798–.916)	0.637 _(.369–.842)	0.561 _(.316–.788)	0.747 _(.585–.888)	0.623 _(.456–.778)
	CheXFound	0.209 _(.204–.214)	0.799 _(.794–.804)	0.620 _(.630–.727)	0.876 _(.860–.892)	0.974 _(.949–.992)	0.967 _(.935–.990)	0.988 _(.939–1.0)	0.990 _(.952–1.0)	0.918 _(.826–.975)	0.856 _(.741–.948)
GLoRI head	PubMedCLIP [29]	0.116 _(.115–.117)	0.649 _(.643–.655)	0.501 _(.450–.552)	0.804 _(.778–.828)	0.897 _(.832–.946)	0.867 _(.807–.927)	0.628 _(.363–.866)	0.694 _(.484–.872)	0.652 _(.483–.810)	0.493 _(.330–.654)
	BiomedCLIP [28]	0.122 _(.121–.123)	0.643 _(.636–.649)	0.552 _(.506–.593)	0.829 _(.809–.847)	0.921 _(.870–.957)	0.897 _(.840–.944)	0.900 _(.738–1.0)	0.898 _(.744–1.0)	0.634 _(.470–.789)	0.505 _(.291–.704)
	CheXzero [13]	0.131 _(.130–.132)	0.671 _(.665–.677)	0.599 _(.551–.647)	0.888 _(.868–.905)	0.912 _(.852–.954)	0.894 _(.838–.942)	0.726 _(.451–.901)	0.653 _(.396–.882)	0.640 _(.467–.807)	0.485 _(.323–.662)
	EVA-X [11]	0.149 _(.147–.150)	0.679 _(.672–.685)	0.614 _(.571–.659)	0.870 _(.853–.888)	0.928 _(.881–.964)	0.896 _(.835–.945)	0.977 _(.909–1.0)	0.979 _(.918–1.0)	0.866 _(.760–.936)	0.748 _(.615–.864)
	RAD-DINO [12]	0.173 _(.171–.176)	0.723 _(.717–.729)	0.639 _(.593–.687)	0.884 _(.869–.898)	0.909 _(.854–.952)	0.885 _(.823–.936)	0.909 _(.747–1.0)	0.911 _(.782–1.0)	0.683 _(.503–.861)	0.615 _(.440–.783)
	CheXFound	0.252 _(.247–.258)	0.830 _(.826–.834)	0.679 _(.630–.727)	0.908 _(.894–.921)	0.983 _(.960–.996)	0.978 _(.951–.995)	1.000 _(1.0–1.0)	1.000 _(1.0–1.0)	0.986 _(.956–1.0)	0.975 _(.931–1.0)

TABLE III

COMPARISON OF CHEXFOUND WITH THE END-TO-END TRAINED MODEL AND VISION-LANGUAGE FOUNDATION MODELS. VALUES INSIDE THE PARENTHESES INDICATE THE 95% CONFIDENCE INTERVALS. VALUES IN **BOLD** INDICATE THE BEST RESULTS.

Classifier	Foundation	CXR-LT 24		CheXpert		Shenzhen		Montgomery		JSRT	
		AUPRC	AUROC	AUPRC	AUROC	AUPRC	AUROC	AUPRC	AUROC	AUPRC	AUROC
End-to-end	ConvNeXt [43]	0.170 _(.168–.173)	0.761 _(.756–.766)	0.657 _(.608–.704)	0.886 _(.867–.903)	0.923 _(.870–.963)	0.891 _(.823–.945)	0.622 _(.362–.862)	0.670 _(.458–.872)	0.750 _(.586–.886)	0.608 _(.456–.761)
Img-text align.	PubMedCLIP [29]	0.068 _(.068–.069)	0.531 _(.524–.537)	0.255 _(.221–.294)	0.582 _(.550–.618)	0.577 _(.457–.700)	0.540 _(.437–.637)	0.440 _(.246–.672)	0.426 _(.216–.658)	0.596 _(.426–.758)	0.403 _(.244–.572)
	BiomedCLIP [28]	0.071 _(.071–.072)	0.539 _(.533–.545)	0.356 _(.317–.393)	0.653 _(.626–.681)	0.795 _(.705–.878)	0.760 _(.680–.836)	0.786 _(.567–.936)	0.714 _(.487–.912)	0.692 _(.516–.859)	0.554 _(.397–.722)
	CheXzero [13]	0.134 _(.133–.136)	0.668 _(.662–.674)	0.646 _(.600–.692)	0.888 _(.868–.905)	0.875 _(.804–.933)	0.849 _(.776–.911)	0.967 _(.870–1.0)	0.969 _(.889–1.0)	0.708 _(.532–.863)	0.530 _(.378–.698)
GLoRI head	CheXFound	0.252 _(.247–.258)	0.830 _(.826–.834)	0.679 _(.630–.727)	0.908 _(.894–.921)	0.983 _(.960–.996)	0.978 _(.951–.995)	1.000 _(1.0–1.0)	1.000 _(1.0–1.0)	0.986 _(.956–1.0)	0.975 _(.931–1.0)

model (either RAD-DINO or EVA-X) by 9.5% ($p < 0.001$, two-sided paired permutation test). On the five-class multilabel classification task (CheXpert), CheXFound outperformed the next best-performing model (EVA-X) by 8.8% ($p < 0.001$) in AUROC. On single-class classification tasks (Shenzhen, Montgomery, and JSRT) with limited amounts of training data, CheXFound similarly outperformed the next best-performing models in AUROC by 11.7% ($p < 0.001$), 42.9% ($p < 0.001$), and 23.3% ($p < 0.001$), respectively.

We further evaluated the performance of the foundation models using GLoRI across five classification tasks (Table II). The foundation models (CheXFound, RAD-DINO, EVA-X, CheXzero, BiomedCLIP, and PubMedCLIP) with GLoRI generally outperformed their linear probe baselines. Specifically, CheXFound with GLoRI outperformed its linear probe baseline in AUROC by 3.1%, 3.2%, 1.1%, 1.0%, and 11.9% on CXR-LT 24, CheXpert, Shenzhen, Montgomery, and JSRT, respectively. CheXFound with GLoRI also outperformed other foundation models, including CLIP-based models (CheXzero, BioMedCLIP, and PubMedCLIP) under image-text alignment, as well as end-to-end trained ConvNeXt (Table III).

To show the detailed performance of CheXFound over 40 disease findings, we illustrated CheXFound performance in AUROC against its comparisons in Fig. 3. CheXFound consistently outperformed other methods across the 40 disease findings in AUROC. We also compared performance in AUPRC over disease findings with high, medium, and low prevalence

in Fig. 3b. CheXFound outperformed its comparisons under all levels of prevalence, even for underrepresented pathologies in the low prevalence category.

B. Opportunistic predictive power

Beyond thoracic disease detection tasks, we evaluated CheXFound’s generalizability in opportunistic CXR interpretation. For this purpose, we requested access to the CXR arm of the PLCO trial [46], which includes digitally scanned CXR films and up to 25-year mortality follow-up data. Using this dataset, we investigated CheXFound’s predictive capability for cardiovascular disease (CVD) risk and all-cause mortality estimation. We used CheXFound with ViT-L pretrained on CXR-1M in this experiment and compared CheXFound against two vision foundation models (RAD-DINO, EVA-X) and the end-to-end trained model, ConvNeXt.

CheXFound consistently outperformed its counterparts in both CVD risk and all-cause mortality estimation tasks. CheXFound achieved 0.749 for CVD risk estimation and 0.786 for all-cause mortality estimation in AUROC, significantly outperforming the next best-performing method (ConvNeXt) by 3.5% ($p < 0.001$) and 4.1% ($p < 0.001$), respectively. For the all-cause mortality estimation task, we divided the test cohort into low-risk and high-risk groups based on the model prediction and computed their Kaplan-Meier curves (Fig. 5). The survival distributions for the low-risk and high-risk groups are statistically different ($p < 0.001$, log-rank test).

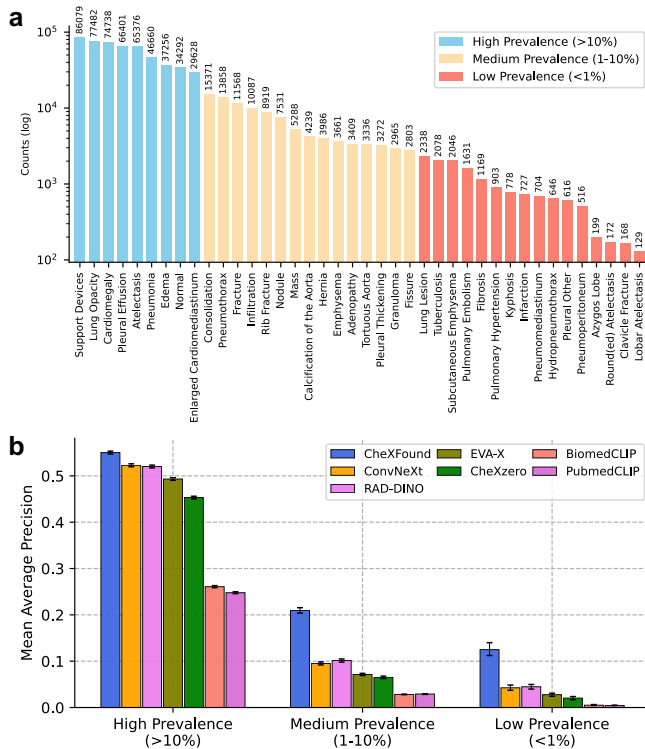


Fig. 4. Model performance under high, medium and low disease prevalence. **a**, The number of labels for the 40 disease findings on the CXR-LT 24 dataset [22]. **b**, Model performance in AUPRC stratified by high, medium and low disease prevalence. Error bars indicate the 95% confidence intervals of AUPRC over 1,000 bootstrapped samples.

TABLE IV

MODEL PERFORMANCE ON CVD RISK AND ALL-CAUSE MORTALITY ESTIMATION. VALUES INSIDE THE PARENTHESES ARE 95% CONFIDENCE INTERVALS. VALUES IN **BOLD** INDICATE THE BEST-PERFORMING RESULTS.

Methods	CVD risk		All-cause mortality	
	AUPRC	AUROC	AUPRC	AUROC
ConvNeXt [43]	0.249 _(.240–.257)	0.714 _(.705–.723)	0.638 _(.629–.646)	0.745 _(.736–.753)
EVA-X [11]	0.179 _(.171–.188)	0.643 _(.635–.652)	0.545 _(.536–.554)	0.680 _(.674–.686)
RAD-DINO [12]	0.223 _(.215–.231)	0.687 _(.679–.695)	0.615 _(.607–.622)	0.723 _(.716–.729)
CheXFound	0.289 _(.276–.301)	0.749 _(.741–.756)	0.695 _(.687–.702)	0.786 _(.782–.791)

The end-point survival probabilities are also different by a large margin for low-risk and high-risk groups (78.4% versus 38.4%). Overall, we demonstrated CheXFound generalization capability for opportunistic CXR interpretation.

C. Scalability of self-supervised vision encoders

The scaling capabilities of the self-supervised vision encoders depends on both the model size and the pretraining data size and diversity [21], [26]. To analyze the scaling trends, we pretrained CheXFound across a range of data scales, with CXR-1M and its two subsets CXR-744K and CXR-207K. We also evaluated the impact of model scale by using ViT-Base (ViT-B) and ViT-Large (ViT-L) as the backbones.

Our results in Table V demonstrate that CheXFound benefits from both data and model scaling. Increasing the pretraining

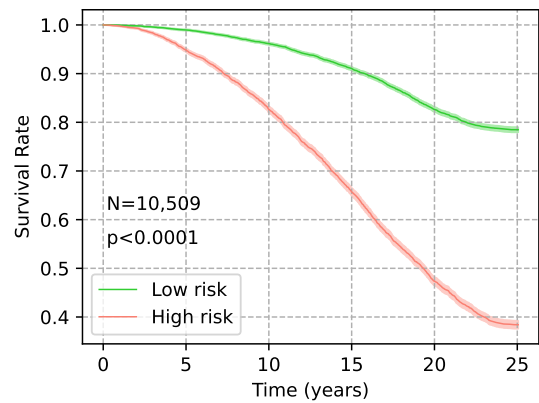


Fig. 5. Kaplan-Meier curves for low-risk and high-risk groups of all-cause mortality on the PLCO dataset. The number of subjects in the test set is 10,509. The survival rates for low-risk and high-risk groups are significantly different ($p < 0.0001$, log-rank test). Shaded areas indicate 95% confidence intervals.

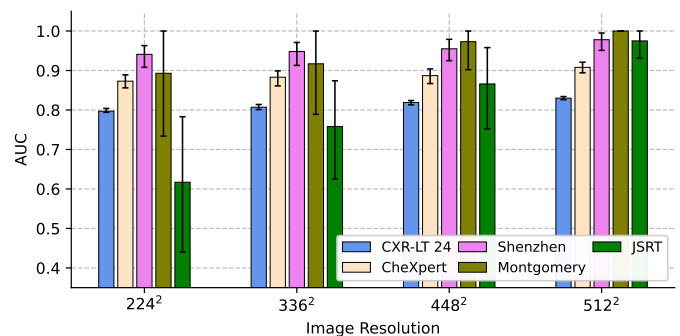


Fig. 6. Evaluation of CheXFound model on the CXR-LT 24, CheXpert, Shenzhen, Montgomery, and JSRT datasets across a range of pretraining image resolutions. Error bars indicate 95% confidence intervals.

data from CXR-207K to CXR-1M with a ViT-L backbone leads to significant AUROC improvements of 3.5% ($p < 0.001$) on CXR-LT 24, 3.4% ($p < 0.001$) on CheXpert, 3.8% ($p < 0.001$) on Shenzhen, 6.8% ($p < 0.001$) on Montgomery, and 30.7% ($p < 0.001$) on JSRT. We observed similar trends when using ViT-B, with performance also improving as we scale up the pretraining data from CXR-207K to CXR-1M. In addition, CheXFound with ViT-L consistently outperformed the ViT-B architecture across different data sizes. These results align with previous studies on scaling ViT models [12], [21], [26].

D. Impact of CXR resolution

To assess the impact of CXR resolution used for pretraining, we pretrained CheXFound using ViT-L with a patch size of 16 across a range of input resolution, including 224^2 , 336^2 , 448^2 , and 512^2 . We empirically found that pretraining at high resolution from scratch cannot produce meaningful representations for downstream tasks. To deal with this problem, we pretrained CheXFound at resolution 224^2 from scratch and then used the pretrained weights to initialize higher-resolution pretraining at 336^2 , 448^2 , and 512^2 .

Fig. 6 shows that self-supervised pretraining at higher resolutions results in improved performance on downstream

TABLE V

MODEL PERFORMANCE ACROSS PRETRAINING DATA SIZES AND MODEL SCALES. RESULTS ARE GIVEN IN THE MEAN VALUES OF AUPRC AND AUROC OVER 1000 BOOTSTRAPPED SAMPLES. VALUES INSIDE THE PARENTHESES INDICATE THE 95% CONFIDENCE INTERVALS. VALUES IN **BOLD** INDICATE THE BEST-PERFORMING RESULTS.

Pretrain.	Arch.	CXR-LT 24		CheXpert		Shenzhen		Montgomery		JSRT	
		AUPRC	AUROC	AUPRC	AUROC	AUPRC	AUROC	AUPRC	AUROC	AUPRC	AUROC
CXR-207K	ViT-Base	0.185 _(.182–.188)	0.775 _(.753–.789)	0.598 _(.550–.645)	0.854 _(.839–.862)	0.921 _(.898–.946)	0.909 _(.855–.953)	0.889 _(.732–1.0)	0.897 _(.742–1.0)	0.756 _(.591–.882)	0.612 _(.495–.712)
	ViT-Large	0.207 _(.203–.210)	0.795 _(.774–.813)	0.618 _(.629–.726)	0.874 _(.862–.884)	0.953 _(.923–.979)	0.940 _(.901–.962)	0.923 _(.811–1.0)	0.932 _(.826–1.0)	0.775 _(.620–.892)	0.668 _(.537–.784)
CXR-744K	ViT-Base	0.211 _(.208–.214)	0.803 _(.792–.810)	0.614 _(.571–.659)	0.869 _(.854–.886)	0.938 _(.913–.961)	0.925 _(.875–.963)	0.909 _(.775–1.0)	0.915 _(.785–1.0)	0.866 _(.759–.935)	0.747 _(.695–.787)
	ViT-Large	0.217 _(.214–.221)	0.813 _(.801–.822)	0.643 _(.596–.692)	0.887 _(.876–.896)	0.964 _(.935–.986)	0.956 _(.923–.972)	0.953 _(.843–1.0)	0.957 _(.845–1.0)	0.905 _(.794–.953)	0.826 _(.674–.925)
CXR-1M	ViT-Base	0.219 _(.215–.223)	0.815 _(.811–.819)	0.632 _(.583–.679)	0.877 _(.853–.896)	0.957 _(.924–.979)	0.947 _(.925–.963)	0.923 _(.788–1.0)	0.927 _(.818–1.0)	0.908 _(.806–.955)	0.845 _(.696–.943)
	ViT-Large	0.252 _(.247–.258)	0.830 _(.826–.834)	0.679 _(.630–.727)	0.908 _(.894–.921)	0.983 _(.960–.996)	0.978 _(.951–.995)	1.000 _(1.0–1.0)	1.000 _(1.0–1.0)	0.986 _(.956–1.0)	0.975 _(.931–1.0)

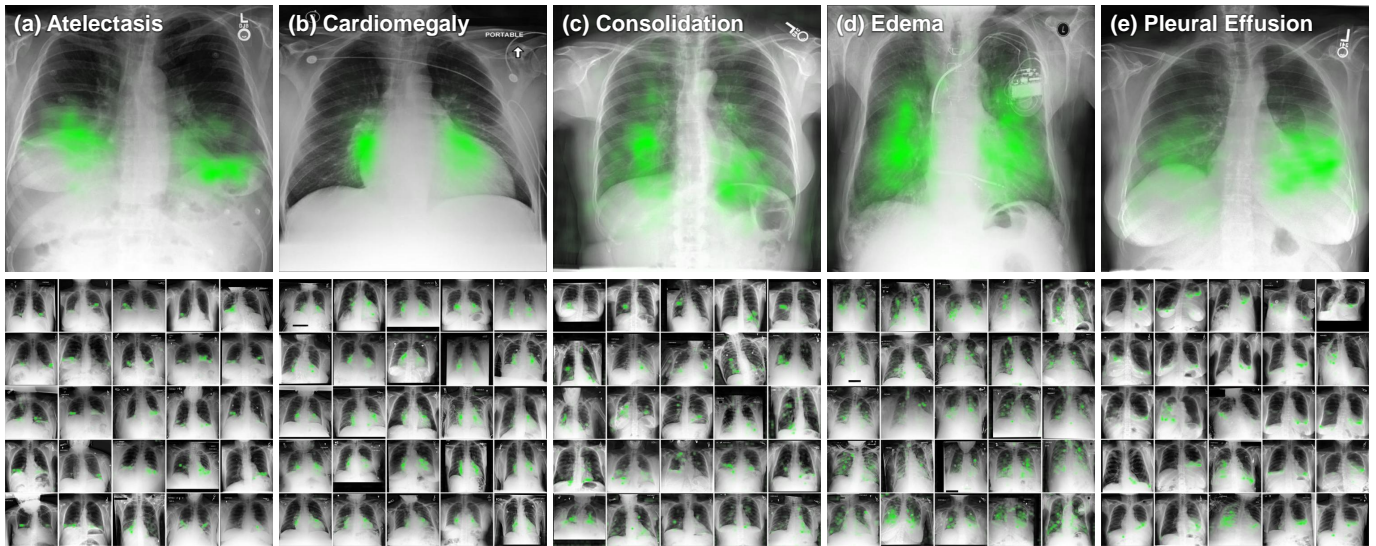


Fig. 7. GLoRI attention maps for disease findings of atelectasis, cardiomegaly, consolidation, edema, and pleural effusion, respectively. Each subfigure contains 25 CXRs with their GLoRI attention maps overlaid (bottom) and an anchor CXR with a global attention map overlaid (top). The global attention maps are the averaged attention maps of 25 CXRs after registered to the anchor image.

tasks. Increasing the pretraining resolutions from 224^2 pixels to 512^2 pixels significantly improves the AUROC by 3.3% ($p < 0.001$), 3.5% ($p < 0.001$), 3.7% ($p < 0.001$), 10.7% ($p < 0.001$), and 35.8% ($p < 0.001$) on the CXR-LT 24, CheXpert, Shenzhen, Montgomery, and JSRT datasets, respectively.

VI. DISCUSSION AND CONCLUSION

A. Interpretation of disease-specific local features

The interpretability of an artificial intelligence model is crucial to its medical applications. In this study, we trained GLoRI on top of the frozen foundation model. GLoRI inherently provides interpretable attention maps for each pathology. We visualized the attention maps for a selection of five pathologies of 25 CXRs and aligned these attention maps to an anchor CXR via affine registration¹ to provide a global perspective in Fig. 7. The attention maps contain precise localization of abnormalities in CXRs and the global attention maps cover the regions where the pathologies constantly occur. To be specific, edema refers to the accumulation of excess fluid and

its abnormal regions often diffuse across lungs. This pattern is well captured by our attention maps as we observed in Fig. 7d that the critical regions in the individual attention maps scatter over the lungs and the global attention map covers extensive regions of both lungs. However, these attention maps have the limitations of covering partial regions of the abnormalities. For example, the attention maps for cardiomegaly only cover the heart on the left and right regions of the spine, and some maps for pleural effusion only cover the inferior boundaries of the lung while ignore the remaining abnormal regions.

B. Generalizability of foundation models

An important characteristic of CheXFound and other foundation models is their generalization capabilities to in-distribution and out-of-distribution downstream tasks. Compared with other encoders, we found that CheXFound achieved better performances on both in-distribution CXR-LT 24 and CheXpert datasets and out-of-distribution Shenzhen, Montgomery, and JSRT datasets. On the opportunistic CXR interpretation tasks on PLCO, CheXFound also achieved consistent and significant increases over comparison methods.

¹We apply affine registration using the SimpleElastix library: <https://simpleelastix.readthedocs.io>.

CheXFound’s generalizability is attributed to the strong representation quality of frozen features learned via pretraining with large-scale, diverse CXRs. We also demonstrated CheXFound’s generalization capabilities on infrequent and underrepresented pathologies. CheXFound achieved significant increases over its comparisons in classifying low-prevalence pathologies with lower than 1% occurrence frequencies, demonstrating its superior label efficiency. Although CheXFound with ViT-L achieved robust generalizability, our study did not evaluate the best-performing ViT-giant (ViT-g) architecture in DINOv2, a larger model with 1.1B parameters, which we expect to achieve better generalization performances in CXR interpretation, but it demands more pretraining data and computational resources. Overall, we demonstrated CheXFound’s robust generalization capabilities, which we believe can enable diverse downstream adaptations with improved label efficiency.

C. Conclusion

In summary, this work introduces CheXFound, a vision-centric foundation model pretrained via self-distillation on over one million unique CXRs. For downstream adaptations, we trained a GLoRI module on top of the frozen CheXFound, which combines disease-specific local features and global image features to improve the multilabel classification performance. CheXFound outperformed previous methods for classifying 40 disease findings on CXR-LT 24, demonstrating superior label efficiency on datasets with limited training labels, and strong generalization capabilities for opportunistic CXR interpretation on PLCO. The disease-specific local features extracted from CheXFound also carry strong interpretability as visualized by the associated attention maps. In our future work, we will continue to explore novel pretraining schemes to further improve the understanding of CXRs by these foundation models.

REFERENCES

- [1] S. Raoof, D. Feigin, A. Sung, S. Raoof, L. Irugupati, and E. C. Rosenow III, “Interpretation of plain chest roentgenogram,” *Chest*, vol. 141, no. 2, pp. 545–558, 2012.
- [2] J. Weiss, V. K. Raghun, K. Paruchuri, A. Zinzuwadia, P. Natarajan, H. J. Aerts, and M. T. Lu, “Deep learning to estimate cardiovascular risk from chest radiographs,” *Annals of Internal Medicine*, vol. 177, no. 4, pp. 409–417, 2024.
- [3] Z. Yang, J. Zhang, G. Wang, M. K. Kalra, and P. Yan, “Cardiovascular disease detection from multi-view chest x-rays with bi-mamba,” in *International Conference on Medical Image Computing and Computer-Assisted Intervention*. Springer, 2024, pp. 134–144.
- [4] J. Weiss, V. K. Raghun, D. Bontempi, D. C. Christiani, R. H. Mak, M. T. Lu, and H. J. Aerts, “Deep learning to estimate lung disease mortality from chest radiographs,” *Nature Communications*, vol. 14, no. 1, p. 2797, 2023.
- [5] A. Pырros, S. M. Borstelmann, R. Mantravadi, Z. Zaiman, K. Thomas, B. Price, E. Greenstein, N. Siddiqui, M. Willis, I. Shulhan *et al.*, “Opportunistic detection of type 2 diabetes using deep learning from frontal chest radiographs,” *Nature communications*, vol. 14, no. 1, p. 4039, 2023.
- [6] X. Chen, S. Xie, and K. He, “An empirical study of training self-supervised vision transformers,” in *Proceedings of the IEEE/CVF international conference on computer vision*, 2021, pp. 9640–9649.
- [7] K. He, X. Chen, S. Xie, Y. Li, P. Dollár, and R. Girshick, “Masked autoencoders are scalable vision learners,” in *Proceedings of the IEEE/CVF conference on computer vision and pattern recognition*, 2022, pp. 16 000–16 009.
- [8] M. Caron, H. Touvron, I. Misra, H. Jégou, J. Mairal, P. Bojanowski, and A. Joulin, “Emerging properties in self-supervised vision transformers,” in *Proceedings of the IEEE/CVF international conference on computer vision*, 2021, pp. 9650–9660.
- [9] J. Zhou, C. Wei, H. Wang, W. Shen, C. Xie, A. Yuille, and T. Kong, “ibot: Image bert pre-training with online tokenizer,” *arXiv preprint arXiv:2111.07832*, 2021.
- [10] S. Azizi, L. Culp, J. Freyberg, B. Mustafa, S. Baur, S. Kornblith, T. Chen, N. Tomasev, J. Mitrović, P. Strachan *et al.*, “Robust and data-efficient generalization of self-supervised machine learning for diagnostic imaging,” *Nature Biomedical Engineering*, vol. 7, no. 6, pp. 756–779, 2023.
- [11] J. Yao, X. Wang, Y. Song, H. Zhao, J. Ma, Y. Chen, W. Liu, and B. Wang, “Eva-x: A foundation model for general chest x-ray analysis with self-supervised learning,” *arXiv preprint arXiv:2405.05237*, 2024.
- [12] F. Pérez-García, H. Sharma, S. Bond-Taylor, K. Bouzid, V. Salvatelli, M. Ilse, S. Bannur, D. C. Castro, A. Schwaighofer, M. P. Lungren *et al.*, “Rad-dino: Exploring scalable medical image encoders beyond text supervision,” *arXiv preprint arXiv:2401.10815*, 2024.
- [13] E. Tiu, E. Talius, P. Patel, C. P. Langlotz, A. Y. Ng, and P. Rajpurkar, “Expert-level detection of pathologies from unannotated chest x-ray images via self-supervised learning,” *Nature Biomedical Engineering*, vol. 6, no. 12, pp. 1399–1406, 2022.
- [14] A. E. Johnson, T. J. Pollard, S. J. Berkowitz, N. R. Greenbaum, M. P. Lungren, C.-y. Deng, R. G. Mark, and S. Horng, “Mimic-cxr, a de-identified publicly available database of chest radiographs with free-text reports,” *Scientific data*, vol. 6, no. 1, p. 317, 2019.
- [15] J. Irvin, P. Rajpurkar, M. Ko, Y. Yu, S. Ciurea-Ilcus, C. Chute, H. Marklund, B. Haghighi, R. Ball, K. Shpanskaya *et al.*, “Chexpert: A large chest radiograph dataset with uncertainty labels and expert comparison,” in *Proceedings of the AAAI conference on artificial intelligence*, vol. 33, no. 01, 2019, pp. 590–597.
- [16] A. Bustos, A. Pertusa, J.-M. Salinas, and M. De La Iglesia-Vaya, “Padchest: A large chest x-ray image dataset with multi-label annotated reports,” *Medical image analysis*, vol. 66, p. 101797, 2020.
- [17] X. Wang, Y. Peng, L. Lu, Z. Lu, M. Bagheri, and R. M. Summers, “Chestx-ray8: Hospital-scale chest x-ray database and benchmarks on weakly-supervised classification and localization of common thorax diseases,” in *Proceedings of the IEEE conference on computer vision and pattern recognition*, 2017, pp. 2097–2106.
- [18] E. P. Reis, J. P. De Paiva, M. C. Da Silva, G. A. Ribeiro, V. F. Paiva, L. Bulgarelli, H. M. Lee, P. V. Santos, V. M. Brito, L. T. Amaral *et al.*, “Brax, brazilian labeled chest x-ray dataset,” *Scientific Data*, vol. 9, no. 1, p. 487, 2022.
- [19] H. Q. Nguyen, K. Lam, L. T. Le, H. H. Pham, D. Q. Tran, D. B. Nguyen, D. D. Le, C. M. Pham, H. T. Tong, D. H. Dinh *et al.*, “Vindr-cxr: An open dataset of chest x-rays with radiologist’s annotations,” *Scientific Data*, vol. 9, no. 1, p. 429, 2022.
- [20] S. Feng, D. Azzollini, J. S. Kim, C.-K. Jin, S. P. Gordon, J. Yeoh, E. Kim, M. Han, A. Lee, A. Patel *et al.*, “Curation of the candid-ptx dataset with free-text reports,” *Radiology: Artificial Intelligence*, vol. 3, no. 6, p. e210136, 2021.
- [21] M. Oquab, T. Darcet, T. Moutakanni, H. Vo, M. Szafraniec, V. Khalidov, P. Fernandez, D. Haziza, F. Massa, A. El-Nouby *et al.*, “Dinov2: Learning robust visual features without supervision,” *arXiv preprint arXiv:2304.07193*, 2023.
- [22] Y. Peng, M. Lin, G. Holste, S. Wang, Y. Zhou, H. Chen, A. Wang, A. E. Flanders, L. A. Celi, Z. Lu, G. Shih, and R. M. Summers, “CXR-LT 2024: Long-tailed, multi-label, and zero-shot classification on chest X-rays,” Apr. 2024. [Online]. Available: <https://doi.org/10.5281/zenodo.10991413>
- [23] W. G. Hocking, P. Hu, M. M. Oken, S. D. Winslow, P. A. Kvale, P. C. Prorok, L. R. Ragard, J. Commins, D. A. Lynch, G. L. Andriole *et al.*, “Lung cancer screening in the randomized prostate, lung, colorectal, and ovarian (plco) cancer screening trial,” *JNCI: Journal of the National Cancer Institute*, vol. 102, no. 10, pp. 722–731, 2010.
- [24] H. Bao, L. Dong, S. Piao, and F. Wei, “Beit: Bert pre-training of image transformers,” *arXiv preprint arXiv:2106.08254*, 2021.
- [25] T. Chen, S. Kornblith, M. Norouzi, and G. Hinton, “A simple framework for contrastive learning of visual representations,” in *International conference on machine learning*. PMLR, 2020, pp. 1597–1607.
- [26] R. J. Chen, T. Ding, M. Y. Lu, D. F. Williamson, G. Jaume, A. H. Song, B. Chen, A. Zhang, D. Shao, M. Shaban *et al.*, “Towards a general-purpose foundation model for computational pathology,” *Nature Medicine*, vol. 30, no. 3, pp. 850–862, 2024.
- [27] J.-B. Grill, F. Strub, F. Altché, C. Tallec, P. Richemond, E. Buchatskaya, C. Doersch, B. Avila Pires, Z. Guo, M. Gheshlaghi Azar *et al.*,

- “Bootstrap your own latent—a new approach to self-supervised learning,” *Advances in neural information processing systems*, vol. 33, pp. 21 271–21 284, 2020.
- [28] S. Zhang, Y. Xu, N. Usuyama, H. Xu, J. Bagga, R. Tinn, S. Preston, R. Rao, M. Wei, N. Valluri *et al.*, “Biomedclip: a multimodal biomedical foundation model pretrained from fifteen million scientific image-text pairs,” *arXiv preprint arXiv:2303.00915*, 2023.
- [29] S. Eslami, G. de Melo, and C. Meinel, “Does clip benefit visual question answering in the medical domain as much as it does in the general domain?” *arXiv preprint arXiv:2112.13906*, 2021.
- [30] Z. Chen, M. Varma, J.-B. Delbrouck, M. Paschali, L. Blankemeier, D. Van Veen, J. M. J. Valanarasu, A. Youssef, J. P. Cohen, E. P. Reis *et al.*, “Chexagent: Towards a foundation model for chest x-ray interpretation,” *arXiv preprint arXiv:2401.12208*, 2024.
- [31] C. Li, C. Wong, S. Zhang, N. Usuyama, H. Liu, J. Yang, T. Naumann, H. Poon, and J. Gao, “Llava-med: Training a large language-and-vision assistant for biomedicine in one day,” *Advances in Neural Information Processing Systems*, vol. 36, 2024.
- [32] L. Yang, S. Xu, A. Sellergren, T. Kohlberger, Y. Zhou, I. Ktena, A. Kiraly, F. Ahmed, F. Hormozdiari, T. Jaroensri *et al.*, “Advancing multimodal medical capabilities of gemini,” *arXiv preprint arXiv:2405.03162*, 2024.
- [33] A. Zawacki, C. Wu, G. Shih, J. Elliott, M. Fomitchev, M. Hussain, ParasLakhani, P. Culliton, and S. Bao, “Siim-acr pneumothorax segmentation,” 2019.
- [34] “Object-cxr - automatic detection of foreign objects on chest x-rays,” JF Healthcare, 2020.
- [35] P. Lakhani, J. Mongan, C. Singhal, Q. Zhou, K. P. Andriole, W. F. Auffermann, P. Prasanna, T. X. Pham, M. Peterson, P. J. Bergquist *et al.*, “The 2021 siim-fisabio-rsna machine learning covid-19 challenge: Annotation and standard exam classification of covid-19 chest radiographs,” *Journal of Digital Imaging*, vol. 36, no. 1, pp. 365–372, 2023.
- [36] Y. Wu, H. Gunraj, C.-e. A. Tai, and A. Wong, “Covidx cxr-4: An expanded multi-institutional open-source benchmark dataset for chest x-ray image-based computer-aided covid-19 diagnostics,” *arXiv preprint arXiv:2311.17677*, 2023.
- [37] “Midrc covidx challenge,” Medical Imaging and Data Resource Center, 2022.
- [38] M. D. L. I. Vayá, J. M. Saborit, J. A. Montell, A. Pertusa, A. Bustos, M. Cazorla, J. Galant, X. Barber, D. Orozco-Beltrán, F. García-García *et al.*, “Bimcv covid-19+: a large annotated dataset of rx and ct images from covid-19 patients,” *arXiv preprint arXiv:2006.01174*, 2020.
- [39] A. Jaegle, F. Gimeno, A. Brock, O. Vinyals, A. Zisserman, and J. Carreira, “Perceiver: General perception with iterative attention,” in *International conference on machine learning*. PMLR, 2021, pp. 4651–4664.
- [40] N. Carion, F. Massa, G. Synnaeve, N. Usunier, A. Kirillov, and S. Zagoruyko, “End-to-end object detection with transformers,” in *European conference on computer vision*. Springer, 2020, pp. 213–229.
- [41] S. Jaeger, S. Candemir, S. Antani, Y.-X. J. Wáng, P.-X. Lu, and G. Thoma, “Two public chest x-ray datasets for computer-aided screening of pulmonary diseases,” *Quantitative imaging in medicine and surgery*, vol. 4, no. 6, p. 475, 2014.
- [42] J. Shiraishi, S. Katsuragawa, J. Ikezoe, T. Matsumoto, T. Kobayashi, K.-i. Komatsu, M. Matsui, H. Fujita, Y. Kodera, and K. Doi, “Development of a digital image database for chest radiographs with and without a lung nodule: receiver operating characteristic analysis of radiologists’ detection of pulmonary nodules,” *American journal of roentgenology*, vol. 174, no. 1, pp. 71–74, 2000.
- [43] Z. Liu, H. Mao, C.-Y. Wu, C. Feichtenhofer, T. Darrell, and S. Xie, “A convnet for the 2020s,” in *Proceedings of the IEEE/CVF conference on computer vision and pattern recognition*, 2022, pp. 11 976–11 986.
- [44] Y. Fang, W. Wang, B. Xie, Q. Sun, L. Wu, X. Wang, T. Huang, X. Wang, and Y. Cao, “Eva: Exploring the limits of masked visual representation learning at scale,” in *Proceedings of the IEEE/CVF Conference on Computer Vision and Pattern Recognition*, 2023, pp. 19 358–19 369.
- [45] A. Radford, J. W. Kim, C. Hallacy, A. Ramesh, G. Goh, S. Agarwal, G. Sastry, A. Askell, P. Mishkin, J. Clark *et al.*, “Learning transferable visual models from natural language supervision,” in *International conference on machine learning*. PMLR, 2021, pp. 8748–8763.
- [46] M. M. Oken, W. G. Hocking, P. A. Kvale, G. L. Andriole, S. S. Buys, T. R. Church, E. D. Crawford, M. N. Fouad, C. Isaacs, D. J. Reding *et al.*, “Screening by chest radiograph and lung cancer mortality: the prostate, lung, colorectal, and ovarian (plco) randomized trial,” *Jama*, vol. 306, no. 17, pp. 1865–1873, 2011.